

# A Nanocrystal Catalyst Incorporating a Surface Bound Transition Metal to Induce Photocatalytic Sequential Electron Transfer Events

Jovan San Martin,<sup>§</sup> Xianghua Zeng,<sup>§</sup> Xihan Chen,<sup>§</sup> Collin Miller, Chuang Han, Yixiong Lin, Nobuyuki Yamamoto, Xiaoming Wang, Sadegh Yazdi, Yanfa Yan, Matthew C. Beard, and Yong Yan\*

Cite This: *J. Am. Chem. Soc.* 2021, 143, 11361–11369

Read Online

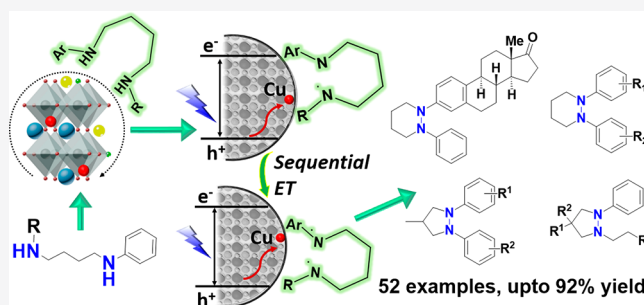
ACCESS |

Metrics & More

Article Recommendations

Supporting Information

**ABSTRACT:** Heterogeneous photocatalysis is less common but can provide unique avenues for inducing novel chemical transformations and can also be utilized for energy transductions, i.e., the energy in the photons can be captured in chemical bonds. Here, we developed a novel heterogeneous photocatalytic system that employs a lead-halide perovskite nanocrystal (NC) to capture photons and direct photogenerated holes to a surface bound transition metal Cu-site, resulting in a N–N heterocyclization reaction. The reaction starts from surface coordinated diamine substrates and requires two subsequent photo-oxidation events per reaction cycle. We establish a photocatalytic pathway that incorporates sequential inner sphere electron transfer events, photons absorbed by the NC generate holes that are sequentially funneled to the Cu-surface site to perform the reaction. The photocatalyst is readily prepared via a controlled cation-exchange reaction and provides new opportunities in photodriven heterogeneous catalysis.



## INTRODUCTION

Heterogeneous catalysis using a renewable energy source may partially address concerns arising from the substantial energy consumption and CO<sub>2</sub> production associated with common and essential chemical process, e.g., the Haber process uses 1–2% of the world's energy supply.<sup>1,2</sup> Lately, heterogeneous electrocatalysis, photocatalysis, and photoelectrocatalysis have gained new attention when renewable energy, i.e., direct solar energy or electrical energy derived from renewable sources, is employed, mainly in the area of N<sub>2</sub> reduction,<sup>3,4</sup> CO<sub>2</sub> reduction,<sup>5–7</sup> water splitting,<sup>8–10</sup> and organic chemical transformations.<sup>11</sup> In addition, under visible light (major component of solar energy), heterogeneous photocatalysts can exhibit unique synthetic pathways. Systems that are being explored include: Metal–Organic-Frameworks;<sup>12</sup> g-C<sub>3</sub>N<sub>4</sub>;<sup>13,14</sup> chalcogenide quantum dots (QDs);<sup>15,16</sup> and other heterogeneous systems.<sup>17</sup> Pb-halide perovskite nanocrystals (NCs), studied here, are also being explored for highly efficient light-driven organic synthesis toward C–C,<sup>18–20</sup> C–O,<sup>21</sup> C–S, or C–P bond formation reactions.<sup>22</sup> Metal-halide perovskite semiconductors are photoactive and support highly efficient charge-separation and charge-migration. One key characteristic of metal-halide perovskite NCs is their easily accessible bandgap-tuning resulting in band-edge tuning via anion-exchange,<sup>23,24</sup> leading to their exploration in unique applications, such as QD light-emitting devices,<sup>25</sup> QD photovoltaics,<sup>26,27</sup> a broader scope of photocatalytic organic synthesis.<sup>21</sup> Cation exchange in NC systems is also widely

explored to produce novel synergistic functional systems and is enhanced in nanocrystalline systems.<sup>28–31</sup> Thus, metal-halide perovskite NCs offer a highly tunable, flexible platform to develop novel heterogeneous catalytic systems.

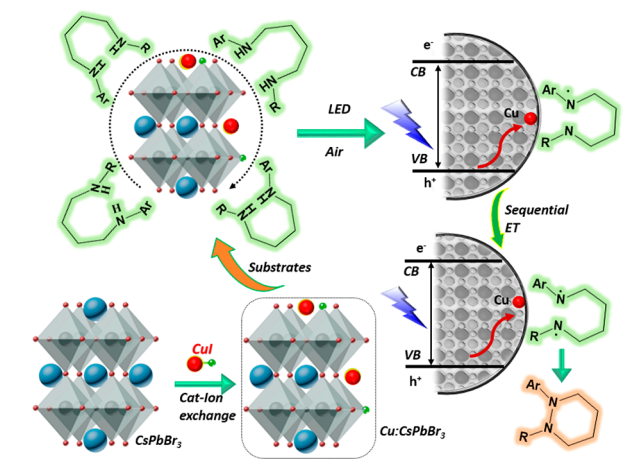
Here, we take advantage of a controlled cation exchange reaction to develop a unique “merged” photocatalysis that employs the NCs as the light absorber and facilitates hole transfer to a transition metal Cu catalyst incorporated onto the NC surfaces as shown in Scheme 1. The photocatalytic NCs are prepared by exposing as-prepared CsPbBr<sub>3</sub> NCs to a solution of Cu(I)X (X = Cl, Br, I) at room temperature, resulting in lightly doped Cu:CsPbBr<sub>3</sub> NCs. The solution-based cation-exchange reaction results in a Cu(I) active site at the NC surface, providing a pathway for ultrafast inner-sphere electron transfer (ET) events (~20 ps illustrated by transient absorption) from the light absorber to the metal center, and represents a distinctive approach from employing a dual cocatalysis system that operates via photoinduced outer sphere ET events.<sup>32</sup> Due to their ability to adopt multiple oxidation states, transition metal compounds are known to be efficient homogeneous and heterogeneous catalysts. Here, our

Received: January 17, 2021

Published: July 21, 2021



### Scheme 1. Photocatalytic Sequential Electron Transfer Approach for Di-Radical Path N-Heterocyclization



hybrid catalyst has both a Cu-active transition metal catalytic center and a photoactive light-absorber. We find that the Cu site serves two important functions: (1) it coordinates the substrate and (2) attracts photogenerated holes from the valence band (VB) of the perovskite NCs leading to the sequential oxidation of the bound substrate. As a result of this unique Cu active site, the heterogeneous photocatalyst can be employed to produce heterocycle N–N complexes with TON (turnover numbers) over 44600.

## RESULTS AND DISCUSSION

**Photocatalysts Development.** We synthesized the perovskite NCs, in the size range of 10–20 nm (see Methods, SI Section 1 and Figure 1a,b), according to previously published methods.<sup>18,21</sup> To prepare the cation-exchanged NCs, the as-produced NCs are mixed with a CuBr salt in toluene. On the basis of the HRTEM and fast Fourier transform images (Figure 1b), the crystalline lattice constant for the (100) planes contract to 0.578 nm upon Cu incorporation, matching a previous report.<sup>28</sup> In agreement with previous observations,<sup>34</sup> we observe an immediate photoluminescence (PL) quenching and a blue-shift upon addition of the CuBr (Figure 1c). Changes in absorption onset (Figure 1d) are consistent with the observed PL shift. Halide exchange also occurs, and when only the halide is exchanged, there is a resulting red (when X = I) or blue-shift (X = Cl) of the PL. (SI Section 1) However, in our experiments, we find that the PL blue-shifts for each of the Cu(I) salts irrespective of the anion, with CuCl exhibiting the largest blue-shift and CuI the smallest. Thus, Cu incorporation results in a blue-shifted PL. The PL results indicate that both Cu and the halide are incorporated into the NCs in agreement with literature reports.<sup>21,23,24</sup>

We infer that Cu(I) likely replaces Cs via X-ray diffraction (XRD, Figure 1e,f) in conjunction with density-functional theory (DFT) simulations, Energy-Dispersive X-ray Spectroscopy, (EDS, Figure 1g–l), and electron paramagnetic resonance (EPR) experiments (see method and SI Section 2). A lattice contraction is observed by a shift to larger  $2\theta$  values in the powder XRD (Figure 1e,f) resulting from the

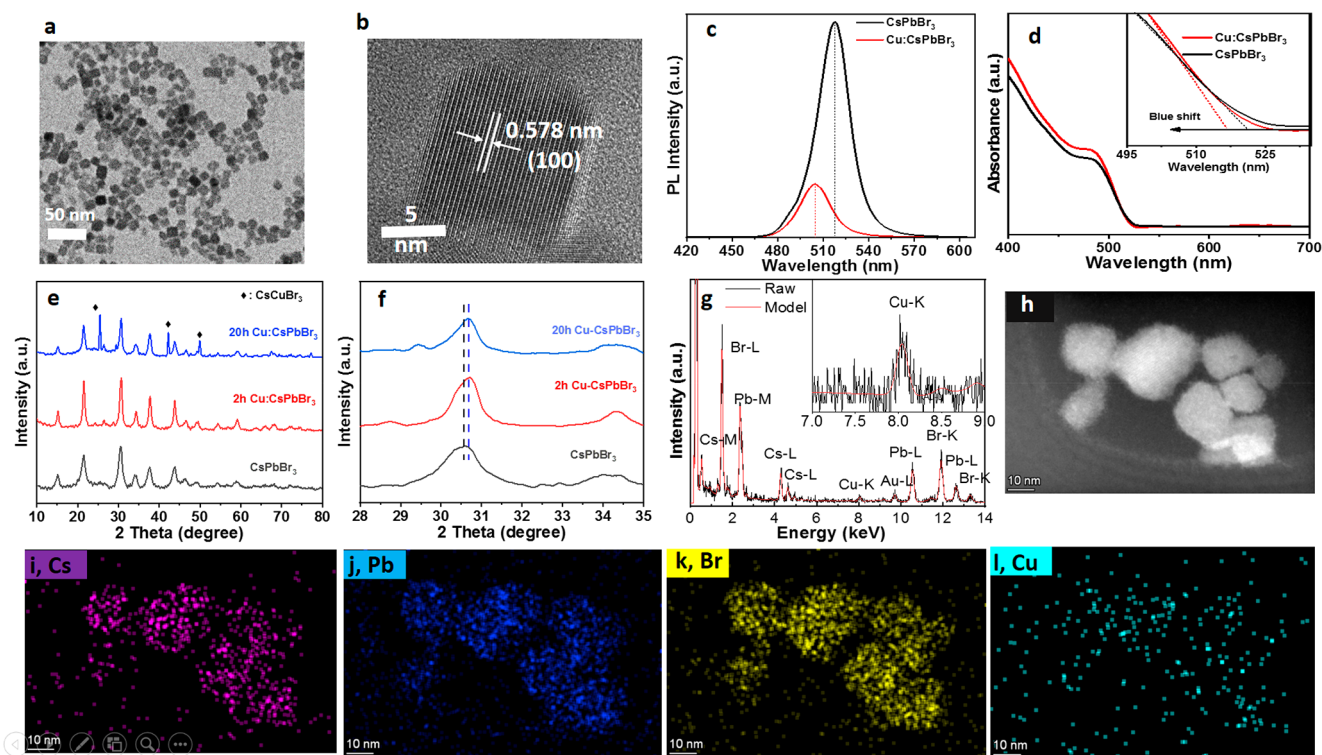


**Figure 1.** Structural and optical characterization of CuBr-exchanged CsPbBr<sub>3</sub>NCs. (a) TEM. (b) HR-TEM. (c) Photoluminescence (PL), excited at 400 nm for as prepared CsPbBr<sub>3</sub> NCs (dark), treated with CuBr (red). (d) Linear absorption near the bandedge showing similar shifts in absorption onset as observed in PL. (e) XRD comparisons, (100) Miller indices at  $\sim 15^\circ$ , (200) at  $\sim 30^\circ$ , and (211) at  $\sim 37^\circ$ . (f) Enlarged-view comparison of the (200) peak position indicating contraction of the lattice upon Cu incorporation. (g) EDS mapping, inset shows the enlarged-view of Cu, note the Au residue due to the gold grid. (h) EDS image area. (i) Cs content. (j) Pb, (k) Br, and (l) Cu. The amount of Cu detected is consistent with  $\sim 1\%$  loading of Cu.

smaller radius of Cu(I) compared to Cs.<sup>33</sup> The shift in  $2\theta$  becomes more prominent in samples (enlarged view see SI Section 3) that have undergone a larger fraction of Cu(I) cation-exchange and thus exhibit a larger lattice contraction.<sup>28</sup> DFT simulations suggest that Cu(I) substitutes for Cs while Cu(II) would substitute for Pb (see SI Section 4). Here, no Cu(II) is detected (in the absence of light) via EPR measurements and thus we rule out Cu(I) oxidation to Cu(II) during the cation exchange reaction.

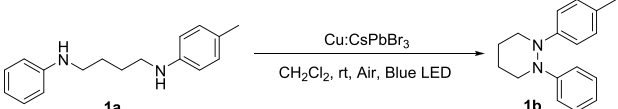
The catalytically active Cu cations reside near or at the NC surface, while any Cu cations that diffuse to the center of the NCs are likely not catalytically active. An accurate determination of the active Cu(I) site on the heterogeneous NC surface would need further characterization and is beyond the scope of this project. However, our results suggest Cu(I) is incorporated into the NC lattice and is electronically coupled to the Pb-halide framework. EDS mapping in Figure 1h–l, shows evidence that Cu atoms are on or in the NCs, but it (Figure 1l) also indicates free Cu atoms are present; however, as we discuss below, free Cu ions in solution are not catalytically active.

**Photocatalytic Reaction.** An intramolecular N–N heterocyclization was explored to probe the catalytic activity of Cu:CsPbBr<sub>3</sub> NC system. Such reactions can be induced directly from surface bound diamine substrates (e.g., **1a**), with ambient air as the terminal oxidant and visible light as the energy source. The cyclative photo-oxidation reactions *via* intramolecular coupling from diamine substrates require consecutive or multiple electron transfer (MET) events, but such multiphoton events have NOT been, so far, photocatalytically achievable. Most photocatalysts are only capable of a photoexcited single electron transfer (SET) event,<sup>35,36</sup> forming a single-radical intermediate, thus, for example, leading to imines,<sup>37–39</sup> azo-complexes,<sup>40,41</sup> or intermolecular N–N couplings.<sup>42,43</sup> A photocatalytic diradical intermediate *via* MET is hence inherently challenging.

The Cu:CsPbBr<sub>3</sub> photocatalyst suspended in dichloromethane under air with 450 nm LED illumination, without any other additives, induces pyridazine **1b** formation from **1a** in 90% yield within 18 h (Table 1). Control experiments omitting any component of the catalytic system, light, or air results in no yield (entry 2–6). To rule out that free Cu in solution does not act as a molecular cocatalyst, we tested if perovskite NCs suspended in the presence of Cu(I), but without sufficient time for ion-exchange, could induce **1b** from **1a** and only found trace amounts of **1b**. (Entry 7)

Free Cu(I) in solution likely coordinates the substrate forming a chelating [Cu(I)(**1a**)<sub>2</sub>]<sup>+</sup> type complex, impeding cation-exchange with perovskite NC and resulting in no reactivity. (SI, Section 1) Under a homogeneous system, **1b** cannot be synthesized using typical molecular photocatalysts, or free Cu in solution as a cocatalyst. In these cases, the reaction would need to proceed through consecutive outer sphere SET events. The first SET induces a single-radical oxidation intermediate and thus it would be challenging for a subsequent photon to induce the intramolecular N–N coupling under our conditions: (entries 8–12) for example, charge transfer to readily formed [Cu(I)(**1a**)<sub>2</sub>]<sup>+</sup> via an outer sphere SET produces [Cu(II)(**1a**)<sub>2</sub>]<sup>2+</sup>. A second SET oxidation step is less likely to occur to a transiently formed [Cu(II)(**1a**)<sub>2</sub>]<sup>2+</sup> but would rather prefer the thermodynamically favored and widely available, in a homogeneous system, another [Cu(I)(**1a**)<sub>2</sub>]<sup>+</sup>. Outer sphere SET, which would

Table 1. Reaction Comparison and Optimization



Entry	Change from Standard Conditions	<b>1b</b> ,% <sup>b</sup>
1	None	90
2	without Cu-CsPbBr <sub>3</sub>	0
3	without Blue LED	0
4	Under N <sub>2</sub> in closed vial	0
5	With CsPbBr <sub>3</sub> instead	0
6	With CuI instead	0
7 <sup>c</sup>	With CsPbBr <sub>3</sub> + CuI	Trace
8 <sup>d</sup>	Ir(ppy) <sub>3</sub> + CuI	0
9 <sup>d</sup>	Ir(ppy) <sub>2</sub> (dtpy) + CuI	0
10 <sup>d</sup>	Ir(dFCF <sub>3</sub> ppy) <sub>2</sub> (dtpy) + CuI	Trace
11 <sup>d</sup>	Ru(bpy) <sub>3</sub> (PF <sub>6</sub> ) <sub>2</sub> + CuI	0
12 <sup>d</sup>	Mes-Acr + CuI	0
13	Cu-CsPbBr <sub>3</sub> exchanged from CuBr	86
14	Cu-CsPbBr <sub>3</sub> exchanged from CuBr <sub>2</sub>	39
15	Cu-CsPbBr <sub>3</sub> exchanged from CuCl	70
16	Cu-CsPbBr <sub>3</sub> exchanged from CuCl <sub>2</sub>	35

<sup>a</sup>Conditions: **1a** (0.1 mmol), Cu:CsPbBr<sub>3</sub> (2 mg), CH<sub>2</sub>Cl<sub>2</sub> (2 mL), room temperature, under air, 18 h. <sup>b</sup>Isolated yield. <sup>c</sup>Directly added, no exchange time. <sup>d</sup>Catalyst ratio 1:1.

operate in a cocatalyst scenario, also favors [Cu(I)(**1a**)<sub>2</sub>]<sup>+</sup> oxidation over transiently formed [Cu(I)(**1a**)(**1a**•)]<sup>2+</sup>, resulting via disproportionation from [Cu(II)(**1a**)<sub>2</sub>]<sup>2+</sup>. Therefore, a MET pathway is not likely for homogeneous or cocatalyst arrangement conditions and is, in fact, not observed under our conditions.

Further exploration of the catalytic performance was conducted using various Cu(I) and Cu(II) halides (entry 1, 13–16). We find that Cu(II)-exchanged NCs (entry 14) are much less active. Cu(I) is readily photooxidized to Cu(II), while further oxidation to Cu(III) is too deep to be reached from the NCs valence band. Overall a 2 h CuI-exchange renders the highest yield of **1b** (entry 1, and Figure 2a). ICP-OES (Inductively Coupled Plasma Optical Emission Spectroscopy), indicates a Cu content of ~1% in the optimized catalyst, noted here as Cu<sub>0.01</sub>:CsPbBr<sub>3</sub> (see SI Section 5). A higher Cu-loading does not necessarily correspond to a higher reactivity, i.e., a 12-h ion-exchange, leading to >5% Cu-incorporation, results in less catalytic activity. The optimal catalytic activity arises from a balanced and synergistic effect of the Cu cation exchange and Cu catalytic activity. Deficient Cu-loading corresponds to a lower number of Cu-catalytic sites and a lower yield. While higher Cu-incorporation results in phase segregation forming CsCuX<sub>3</sub> rather than further substitution of Cu in the CsPbBr<sub>3</sub> NCs as evidenced by the emerging CsCuX<sub>3</sub> peaks in the XRD for longer cation exchange times (SI Section 3), here, CsCuX<sub>3</sub> is likely neither catalytically nor optically active.

Under our ion-exchange setup, the exchange reaction time determines the amount of Cu-incorporation, that is, when an excess of Cu(I) is employed but under the same exchange time, i.e., two hours, we find the same photocatalytic activity (yield of **1b**, Figure 2b). Overall, only cation-exchanged Cu sites are responsible for the catalytic reaction observed here, and a Cu<sub>0.01</sub>:CsPbBr<sub>3</sub> appears to be optimal. Reuse of the catalyst through centrifugation is achievable for at least four

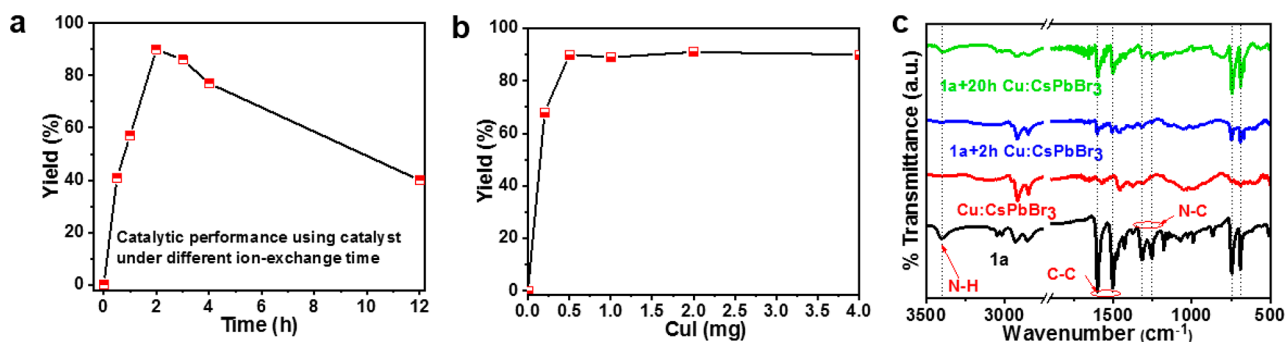


**Figure 2.** Mechanistic exploration. (a) Optimized Cu loading for yield of **1b**; 0.5 mg CuI per 2 mg NCs used for ion-exchange under different time. (b) Catalytic performance using excess CuI for ion-exchange with 2 mg NCs under 2h ion-exchange time. (c) FTIR comparison indicating the surface binding of substrate through Cu.

cycles rendering a catalytic TON of up to 44600 based on Cu for **1b** production. (see Methods).

**Inner Sphere Consecutive Electron Transfer.** The challenge for oxidative *intramolecular* N–N coupling originates from the diradical formation that must occur on a single diamine molecule. Note that the production of two singly oxidized diamines in solution does not yield the observed heterocyclic product but rather produces *intermolecular* N–N coupling products that are not observed. Thus, consecutive inner sphere charge transfer events from the NC VB to the Cu(I) orbitals followed by charge-transfer to a surface-bound substrate lead to the key intermediate for diradical formation, rendering the *intramolecular* N–N product formed directly from the diamine starting materials.

To achieve this photocatalytic activity, we propose that the diamine substrate coordinates to Cu-sites on the surface of the perovskite NCs such that sequential excitation of the NC leads to the diradical formation. Direct evidence of the diamine coordinating to Cu surface sites is suggested via an IR comparison between pristine CsPbBr<sub>3</sub> and Cu-exchange NCs after mixing with the substrate (Figure 2c). There are clear C–C stretching modes at ~1500 cm<sup>-1</sup>, C–H bending modes at 2500 cm<sup>-1</sup>, N–C stretching modes at 1250 cm<sup>-1</sup>, and N–H stretching mode at 3400 cm<sup>-1</sup> that are present only for **m-2** (after centrifugation) whereas no adsorbed substrate is detected via FTIR in the system without Cu. Furthermore, the IR response associated with the diamine increases when a higher loading of Cu-exchanged samples are employed. The coordinated NC is labeled **m-2** in the photocatalytic cycle proposed in Figure 3.

The coordination complex, **m-2**, facilitates the sequential oxidation of the substrate, i.e., **m-4** to **m-6**. In our mechanism, photoexcited **m-2** undergoes sequential inner sphere MET events to induce the consecutive oxidation of the diamine. Transient absorption (TA) spectroscopy was used to study the mechanism and determine the time scale for hole localization and the subsequent oxidation of the substrate. We compare the TA spectra (Figure 4a) and TA kinetics (Figure 4b) of as-synthesized CsPbBr<sub>3</sub> NCs (black-traces), 1% Cu-doped CsPbBr<sub>3</sub> NCs (red), and Cu-doped NCs in the presence of substrate **1a** (blue) under N<sub>2</sub> to examine the behavior of photogenerated carriers. Changes in the TA spectra likely correspond to charge separation that has been observed in previous experiments.<sup>44</sup> Transient kinetics at the center of exciton peak indicates a very fast charge localization (<1 ps) for Cu-doped NCs vs CsPbBr<sub>3</sub> NCs. (Comparison of the early decay of black vs red-traces; see SI Section 7 for kinetic

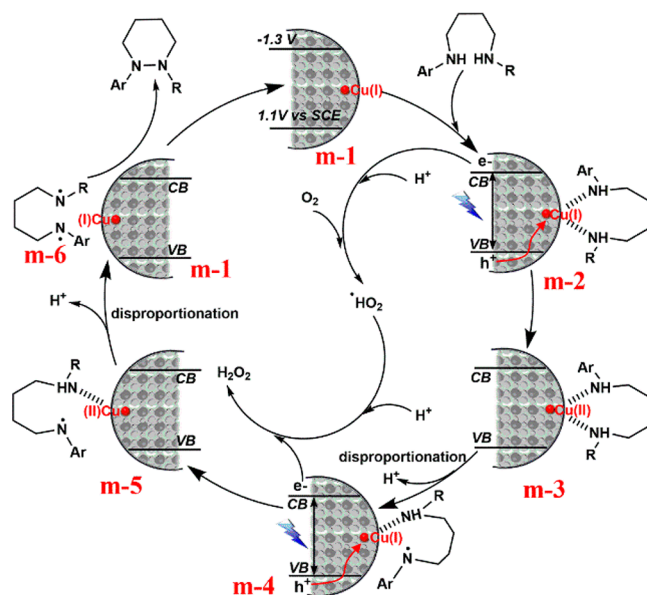


**Figure 3.** Proposed sequential charge transfer reaction mechanism.

analysis). We assign this 0.5 ps decay to hole-localization on the Cu site forming Cu(II), **m-3**, consistent with DFT simulations that place the Cu(I) d-orbitals ~300 meV above the VB of CsPbBr<sub>3</sub> (SI Section 4).

The formation of Cu(II) upon light illumination is further confirmed by *in situ* EPR experiments (Figure 4c). Cu(II) has a d<sup>9</sup> electronic configuration and thus exhibits a strong EPR response while Cu(I) (d<sup>10</sup>) is EPR silent.<sup>45</sup> For our reaction mixture, before light illumination there is no EPR signal, corroborating the proposed Cu(I) surface doping discussed above (i.e., Cu replaces Cs). We have also performed TA measurements in air to examine the reaction pathway (SI Section 7), the observed kinetics are nearly invariant when compared with the N<sub>2</sub> kinetics at early time delays (<100 ps). This is an indication that the Cu(II) formation is likely due to photogenerated holes localization and not O<sub>2</sub>-induced oxidation. The observation that the hole- rather than O<sub>2</sub>-induced Cu(I) oxidation is also corroborated with EPR control experiments, where Cu:CsPbBr<sub>3</sub> under air, but without **1a**, results in no EPR signal under light. Further, when the light is blocked, the EPR signal goes back to zero (Figure 4c, green trace).

With the addition of the substrate **1a**, we find an additional decay channel in the TA kinetics with a time constant of

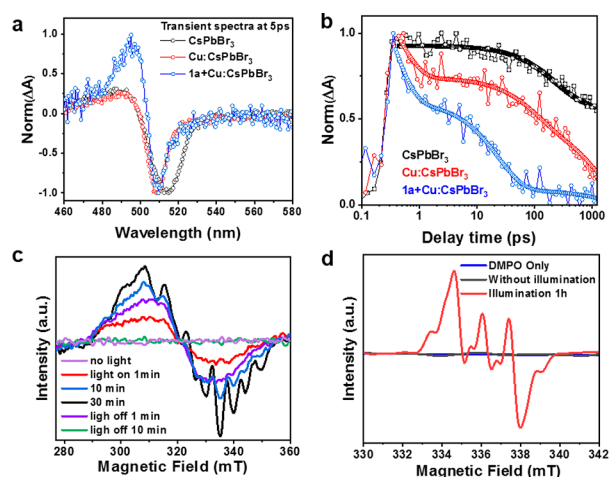


**Figure 4.** Transient spectra and kinetics of perovskite nanocrystals (NCs) and 1% Cu doped NCs (Cu NCs). (a) Transient spectra at 5 ps delay and (b) Transient kinetics with fits at the center of exciton peak of pure perovskite nanocrystals (NCs, black), Cu doped perovskite nanocrystals (Cu NCs, blue) and Cu doped perovskite nanocrystals with substrates **1a** excited with 480 nm (2.6 eV) pump pulse under  $N_2$ . (Cu NCs+sub, green). (c) *In-situ* EPR evidence of Cu(II) formation upon light illumination and disappearance when the light is blocked. (d) *In-situ* EPR evidence of DMPO trapped N-radical.

around 20 ps (Figure 4b, blue-trace compared to red-trace). Since the TA spectra indicates a charge separated state (blue-curve in Figure 4a), this faster decay is assigned to Cu(II) disproportionation to Cu(I), transferring a hole to the substrate and forming **m-4**, likely precluding further hole accumulation on Cu(II) to form Cu(III). The fast time scale of the substrate oxidation supports the assignment of an inner sphere charge transfer to the Cu-coordinated substrate.<sup>20,46</sup> This fast charge transfer is also supported by electrochemical data (SI Section 8) where oxidation potentials of the diamine substrate are located above that of Cu d-orbitals. The Cu(II) EPR response gradually disappears when the incident light is blocked, providing further evidence for our proposed Cu(II) disproportionation in the catalytic cycle.

We can readily deduce from these TA measurements that a second absorbed photon (during the catalytic reaction) would follow the same pathway to form Cu(II), **m-5**, that again disproportionates regenerating Cu(I) and the diradical (**m-6**) which is the key intermediate for N–N heterocyclization. In further support, DMPO (5,5-dimethyl-1-pyrroline-*N*-oxide) is commonly employed in EPR experiments to directly monitor *in situ* radical intermediates.<sup>45</sup> *In-situ* EPR spectra of our reaction mixture with DMPO indeed provides evidence of our proposed N-radical via its characteristic signal (Figure 4d). Regeneration of the perovskite-NC can be achieved via electron transfer from CB to  $O_2$  as demonstrated previously.<sup>21</sup> This is supported by the fact that no reaction is observed in the absence of oxygen (Table 1, entry 4), and the DFT simulations place the  $O_2$  reduction potential to be  $\sim 200$  meV below the CB. Thus, photogenerated holes rapidly oxidize Cu(I) to Cu(II), whereas the photogenerated electrons reduce  $O_2$ .

The production of the key diradical intermediate **m-6** is confirmed via a radical trapping experiment with butylated hydroxytoluene (BHT), a common radical-trapping reagent<sup>47</sup> (see SI Section 9 for details). When BHT is employed to interfere with the reaction, the diradical trapping complex **7c**

was isolated and characterized with Nuclear Magnetic Resonance (NMR), Mass Spectrometry (MS), and single-crystal X-ray crystallography (Figure 5 and details in SI

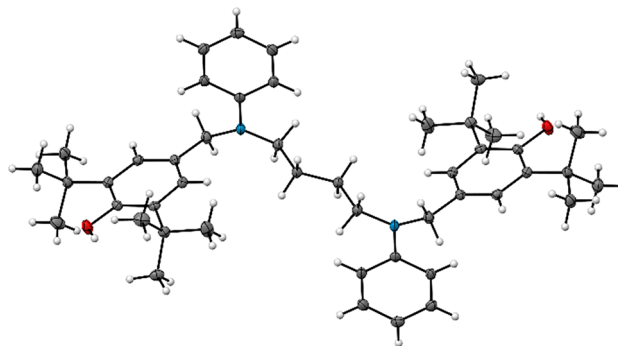


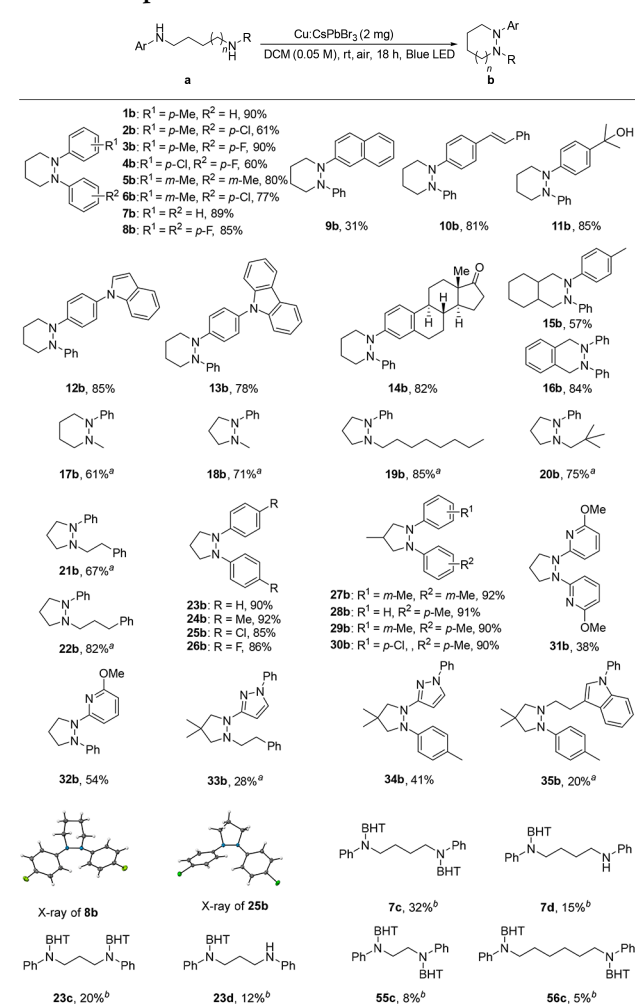
**Figure 5.** Crystal structure of diradical **m-6** trapped intermediate **7c**. (50% Thermal Ellipsoids)

Sections 10–12). Note that monoradical BHT-trapping **7d** is also observed in the MS and NMR but with a much smaller amount providing further evidence for the proposed pathway since some may dissociate from **m-4** or **m-5**. MET events toward a similar diradical formation, as proposed here, have been observed on graphite electrodes in an electrochemical heterogeneous catalytic system.<sup>48,49</sup>

Our ion-exchanged heterogeneous approach via inner sphere MET events provides a unique strategy toward photodriven diradical pathways whereas homogeneous photocatalysts are likely not able to achieve that. Rather, oxidation of aryl/alkyl amines may lead to imines,<sup>37–39</sup> azo-complexes,<sup>40,41</sup> or intermolecular coupling via SET<sup>42,43</sup> in homogeneous systems. Mild conditions (room temperature under air; entries 8–12) lead to low conversion of substrate **1a** when a homogeneous photocatalyst was employed with a Cu(I)-catalyst. Under 1 atm  $O_2$  environment in an elevated temperature, dealkylative azobenzenes are observed (SI Section 13). In accordance, the diradical trapping experiment using molecular photocatalysts, as a control, yielded no **7c** product. Excited state oxidative potentials, (i.e., entries 10, 12) even significantly higher than the VB of the perovskite NCs (or the Cu intermediate), still result in a single-radical which may readily convert to an imine via dehydrogenation,<sup>37–39</sup> an azo-complex via dealkylation<sup>39–41,50,51</sup> or an intermolecular N–N coupling<sup>40–43</sup> as discussed above. The key to our heterogeneous catalytic system is the coordination of the diamine to the Cu heterogeneous environment allowing for multiple charge transfer events.

**Scope of Reaction.** We explored the scope of this heterogeneous photocatalysis. As shown in Table 2, N–N heterocyclizations are widely successful toward pyridazine and 5-member pyrazolidines with 52 examples (**36b–52b**; see SI Section 14) Notably, symmetrical and unsymmetrical couplings, aryl–aryl or aryl–alkyl scaffold, and products of various functional groups on substituted aryls or alkyls or on N–N rings are obtained. Biorelevant **14b** or medically crucial Lewis-basic nitrogen heterocycle tolerant molecules, i.e., indole **12b**, carbazole **13b**, pyridine **31b** and **32b**, pyrazole **33b** and **34b**, tryptamine **35b** are also produced in 20–85% isolated yield.

Sterically hindered heterocycles, i.e., 4- or 8-member rings, are not successful; however, their respective diradical BHT-

Table 2. Scope of Reaction<sup>c</sup>

<sup>a</sup>Cu-CsPbBr<sub>3</sub> (4 mg), 48 h. <sup>b</sup>BHT (1eq) added for trapping. <sup>c</sup>**36b–52b** in SI Section 14.

trapping products **55c–56c** are validated. We suspect the ring closure for diradical **m-6** is not kinetically favored due to a strained pathway; this results in a failure of the diradical coupling. This is proved by the different level of BHT-trapping efficiency in which rates for closure of 5-member rings are fast, resulting in both ring-closure product **23b**, di(**23c**), and mono-BHT (**23d**) trappings (SI Section 9). While the rates for other products are slower, BHT inhibits ring-closure product completely but results in trapping products only. Interestingly, the di-BHT trapping product **7c** is in significantly higher concentration than the mono-BHT trapping **7d** in the case of 6-member rings, while the reverse is true for other cases. Therefore, in addition to strain, lower concentration of the diradical intermediate may also account for the failure of N–N coupling in strained rings.

Overall, electron withdrawing substrates are still challenging because they demonstrate a much higher oxidation potential as shown by the cyclic voltammetry. (SI Section 8) The high oxidation potential of these substrates may impede the disproportionation of Cu(II) (**m-3** or **m-5**) for Cu(I) regeneration, inhibiting inner sphere charge transfer from Cu(II) to the substrate, thus resulting in no reactivity. Further band-tuning of the photocatalyst with Cl<sup>−</sup>, indeed, significantly deepens the VB of the NCs into a more oxidative potential

than these substrates but still results in no yield. (SI Section 15) This likely occurs because charge transfer from VB to Cu(I) is already facile. Anion-tuning of the perovskite NCs should not alter the Cu(II)/Cu(I) potential where the disproportionation is still impeded, resulting in little impact toward these substrates activation.

## CONCLUSION

In summary, we have developed a transition metal merged heterogeneous photocatalytic system for a selective intramolecular N–N heterocyclization. N–N heterocyclic motifs are prevalent in natural products, biorelevant complexes, and pharmaceuticals.<sup>52</sup> Therefore, the scientific challenge of achieving a general N–N heterocyclization from green sources is attractive. Catalytic N–N cyclization is challenging, particularly saturated sp<sup>3</sup> C-based N–N rings that are remarkably labile. Previous approaches toward unsaturated N–N rings were limited to five-member heterocycles, stabilization protocols using amide or imine bonds, or  $\pi$ -conjugated N–N bonds, e.g., electrocatalytic N–N coupling to achieve pyrazolidin-3,5-diones,<sup>48,49</sup> a phosphetane redox cycle resulting in indazoles,<sup>53</sup> and transition metal-based catalysis for five-member aromatic N–N heterocycles.<sup>54–61</sup> Furthermore, the traditional retro-synthetic approach for N–N heterocycles include highly carcinogenic stoichiometric hydrazine as a starting material. In contrast, the photocatalytic broad scope N–N bond-forming reactions developed here that occur directly from vastly abundant amines constitutes a green approach. Synthetic avenues toward forming N–N bonds are scarce compared to those of C–C bond-forming reactions, although much more stable azo N=N bonds are synthetically achievable.<sup>50</sup>

Mechanistic exploration has been illustrated to support the unique diradical pathway via consecutive inner sphere charge transfer events. Rationally tuning a heterogeneous catalyst, particularly a photocatalyst, is inherently challenging. However, the hybrid metal-halide perovskite NCs provide an excellent platform for transition metal incorporation via cation-exchange strategies, rendering a simultaneous light-active photocatalysis and a transition metal catalysis for which such strategies would be difficult to employ for other photocatalysts. Metal doping, tuning, or exchanging of lead-halide perovskites are vastly explored in photovoltaics. We are demonstrating here the transformative nature of metal-halide perovskite systems toward a unique MET photocatalyst system. Merging widely applicable transition metal catalysts into a heterogeneous photocatalyst may forge an exceptional catalytic outcome as demonstrated here. We envision that transition metal-tuned perovskite NCs may open an exciting realm in heterogeneous photocatalytic organic synthesis.

## EXPERIMENTAL SECTION

All commercially available reagents and solvents used in this study were purchased from TCI, Fisher or Sigma-Aldrich and used without further purification. Flash column chromatography was performed using 40–63  $\mu$ m silica gel (SiliaFlash F60 from Silicycle). Preparative thin-layer chromatography was performed on silica gel 60 Å F254 plates (20  $\times$  20 cm, 1000  $\mu$ m, SiliaPlate from Silicycle) and visualized with UV light (254/360 nm). NMR were measured on a Varian spectrometer. Chemical shifts are reported in ppm downfield from Me<sub>4</sub>Si by using the residual solvent peak as an internal standard. Spectra were analyzed and processed using MestReNova Ver. 6.2.0–7163. GCMS was performed on an Agilent 7890 with an Agilent HP-5 ms column (15.0 m  $\times$  250  $\mu$ m  $\times$  0.30  $\mu$ m film thickness) and with an

Agilent 5973 mass detector operating at 70 eV. HRMS EI ( $m/z$ ) was tested on a Waters-Micromass QuattroMicro. ICP-OES measurement was conducted with a PerkinElmer Optima 3000 DV.

#### General Procedure for Preparation of Perovskite Catalyst.

CsPbBr<sub>3</sub> nanocrystals (NCs) were synthesized by modifying the hot injection method previously reported.<sup>18–20</sup> First, a Cs-oleate solution was prepared by charging a 100 mL 3-neck flask with Cs<sub>2</sub>CO<sub>3</sub> (0.16 g) along with octadecene (6 mL, ODE) and oleic acid (2.5 mL, OA) and drying for 1 h under a vacuum at 120 °C. The Cs-oleate solution was then followed by N<sub>2</sub> sparging at 150 °C until all of the Cs<sub>2</sub>CO<sub>3</sub> dissolved in ODE. In a separate 100 mL 3-neck flask, 10 mL of ODE and PbBr<sub>2</sub> (0.178 g, 0.486 mmol) was dried for 1 h under a vacuum at 120 °C and subsequently purged with N<sub>2</sub> followed by an injection of both oleylamine (1 mL) and OA (1 mL). Once the Pb salts dissolved, the temperature was raised to 180 °C, and the prepared Cs-oleate solution (2.1 mL) was swiftly injected into the reactor. After five seconds, the yellow-green reaction mixture was cooled by an ice bath and subsequently washed with tert-butanol (10 mL) and ethyl acetate (30 mL). After centrifuging at 9000 rpm for 5 min, a yellow-green precipitate was obtained and air-dried overnight.

**Preparation of Cu:CsPbBr<sub>3</sub> NCs.** A 20 mg portion of CsPbBr<sub>3</sub> NCs were resuspended in toluene (10 mL) followed by the addition of CuBr salt (5 mg), and the mixture was stirred vigorously in the dark for 2 h. The resulting yellow-green solution mixture was centrifuged at 9000 rpm for 5 min. The supernatant was discarded, and the Cu:CsPbBr<sub>3</sub> NCs pellet was dried in a vacuum oven at 50 °C overnight. CuI or CuCl exchanges were performed under the identical conditions; see details in SI Section 1.

**Photocatalytic Reaction Setup.** The amine substrate (0.1 mmol), CH<sub>2</sub>Cl<sub>2</sub> (1.5 mL), Cu:CsPbBr<sub>3</sub> (2 mg), and stirring bar were added to a 4 mL vial under ambient conditions. Then the reaction mixture was irradiated with a Kessil Blue LED (456 nm, distance to the reaction vial ca. 30 cm) at room temperature under an open air atmosphere (attached a 1 mm diameter venting needle into the sealed cap) for 18 h. Upon completion, the reaction mixture was concentrated and the residue was purified by a column chromatography.

The photocatalyst was reused via centrifugation from the reaction mixture (0.5 mmol scale) and was reapplied at the same scale with the substrate (e.g., 1a). The photocatalyst is active for at least four cycles with the yield noted as 84%, 78%, 73%, and 71%. The catalytic turnover number based on Cu was calculated according to the recentrifuge method.

TON = moles of product/mol of Cu =  $[0.5 \text{ mmol} \times (84\% + 78\% + 73\% + 71\%)] / (1\% \times 2 \text{ mg} / 579.8 \text{ g/mol}) = 44600$

**EPR Study.** The reaction mixture containing substrate 7a (0.1 mmol), CH<sub>2</sub>Cl<sub>2</sub> (1 mL) and Cu:CsPbBr<sub>3</sub> (2 mg) was added into an EPR tube (Magnetech MS-5000 (X band)). The reaction mixture was gently bubbled with air for 15 min before the measurement. The reaction mixture was irradiated in situ with the blue LED at room temperature at various times. The EPR measurement was also recorded at different times when the light was blocked. For details, see SI Section 2.

**TA Experiment Setup.** Transient absorption measurement is based on the Ti:sapphire laser amplifier (Coherent Astrella, 800 nm, pulse duration ~60 fs, ~5 mJ/pulse, and 1 kHz repetition rate) and the pump–probe transient absorption spectrometer (Helios, Ultrafast System). The fundamental beam (800 nm) is split in two beams. One beam is sent to an optical parametric amplifier to generate the pump pulse at 480 nm (2.6 eV), and its intensity is attenuated by two neutral density filter wheels. The other 800 nm beam was focused into a sapphire to generate a white light probe. Probe delay can be up to ~3 ns and is tuned by a delay line. The pump and probe are focused and overlapped onto the sample. The probe size is ~200 μm, and pump beam size is ~400 μm. The beam size is defined as the radius of an aperture that contains (1/e<sup>2</sup>) of the total power. The samples are constantly stirred to give reactants enough time to diffuse. In the TA experiment, the excitation density is kept low (~6 nJ/pulse or 7.65 × 10<sup>9</sup> photons/pulse)<sup>20</sup> such that no multiple excitons are generated in the nanocrystals to complicate our reaction kinetics. The nanocrystals

concentration used in the TA experiment is 0.2 mg/mL, and the substrate concentration is kept at 2 mg/mL.

## ■ ASSOCIATED CONTENT

### Supporting Information

The Supporting Information is available free of charge at <https://pubs.acs.org/doi/10.1021/jacs.1c00503>.

General Information and general procedure for preparation of perovskite catalyst, EPR experiment, XRD of long time Cu ion-exchange samples, DFT calculation experiment, ICP-OES measurement, controlled IR experiment to illustrate substrate-absorbed intermediate *m-2*, ultrafast transient absorption study, electrochemical experiment, radical trapping experiment, NMR of key intermediates, mass spectra of key intermediates, X-ray crystallography data of key intermediates, control experiments in homogeneous system, scope table, further banding-tuning of Cu:CsPbBr<sub>3</sub> with TMSCl, general procedure for preparation of substrates, general procedure for photocatalytic N–N Bond coupling, CVs of electrochemical experiment, spectra of <sup>1</sup>H, <sup>13</sup>C, and <sup>19</sup>F NMR spectra, references (PDF)

## Accession Codes

CCDC 1962359, 1968820–1968821, and 2061006 contain the supplementary crystallographic data for this paper. These data can be obtained free of charge via [www.ccdc.cam.ac.uk/data\\_request/cif](http://www.ccdc.cam.ac.uk/data_request/cif), or by emailing [data\\_request@ccdc.cam.ac.uk](mailto:data_request@ccdc.cam.ac.uk), or by contacting The Cambridge Crystallographic Data Centre, 12 Union Road, Cambridge CB2 1EZ, UK; fax: +44 1223 336033.

## ■ AUTHOR INFORMATION

### Corresponding Author

**Yong Yan** – Department of Chemistry and Biochemistry, San Diego State University, San Diego, California 92182, United States; [orcid.org/0000-0001-6361-0541](https://orcid.org/0000-0001-6361-0541); Email: [Yong.yan@sdsu.edu](mailto:Yong.yan@sdsu.edu)

### Authors

**Jovan San Martin** – Department of Chemistry and Biochemistry, San Diego State University, San Diego, California 92182, United States

**Xianghua Zeng** – Department of Chemistry and Biochemistry, San Diego State University, San Diego, California 92182, United States; College of Biological, Chemical Science and Engineering, Jiaying University, Jiaying 314001, China

**Xihan Chen** – National Renewable Energy Laboratory, Golden, Colorado 80401, United States; [orcid.org/0000-0001-7907-2549](https://orcid.org/0000-0001-7907-2549)

**Collin Miller** – Department of Chemistry and Biochemistry, San Diego State University, San Diego, California 92182, United States

**Chuang Han** – Department of Chemistry and Biochemistry, San Diego State University, San Diego, California 92182, United States

**Yixiong Lin** – Department of Chemistry and Biochemistry, San Diego State University, San Diego, California 92182, United States

**Nobuyuki Yamamoto** – Department of Chemistry and Biochemistry, San Diego State University, San Diego, California 92182, United States

**Xiaoming Wang** – Department of Physics and Astronomy, and Wright Center for Photovoltaics Innovation and Commercialization (PVIC), University of Toledo, Toledo, Ohio 43606, United States; [orcid.org/0000-0002-5438-1334](https://orcid.org/0000-0002-5438-1334)

**Sadegh Yazdi** – Renewable & Sustainable Energy Institute, University of Colorado Boulder, Boulder, Colorado 80309, United States; [orcid.org/0000-0002-3470-9398](https://orcid.org/0000-0002-3470-9398)

**Yanfa Yan** – Department of Physics and Astronomy, and Wright Center for Photovoltaics Innovation and Commercialization (PVIC), University of Toledo, Toledo, Ohio 43606, United States; [orcid.org/0000-0003-3977-5789](https://orcid.org/0000-0003-3977-5789)

**Matthew C. Beard** – National Renewable Energy Laboratory, Golden, Colorado 80401, United States; [orcid.org/0000-0002-2711-1355](https://orcid.org/0000-0002-2711-1355)

Complete contact information is available at:

<https://pubs.acs.org/10.1021/jacs.1c00503>

### Author Contributions

<sup>§</sup>These authors contribute equally to this work

### Notes

The authors declare no competing financial interest.

## ACKNOWLEDGMENTS

The photocatalytic organic reaction exploration is supported by NSF award 1851747 to Y. Yan. Hybrid materials design and development is support via the Center for Hybrid Organic Inorganic Semiconductors for Energy (CHOISE) an Energy Frontier Research Center funded by the Office of Science, Office of Basic Energy Sciences within the US Department of Energy. The calculations were performed using computational resources sponsored by the Department of Energy's Office of Energy Efficiency and Renewable Energy and located at the National Renewable Energy Laboratory. The support from the Facility for Electron Microscopy of Materials at the University of Colorado at Boulder (CU FEMM) is acknowledged.

## REFERENCES

- (1) Smith, B. E. Nitrogenase Reveals Its Inner Secrets. *Science* **2002**, *297* (5587), 1654.
- (2) Conti, J. J.; et al. Energy Consumption by End-Use Sector. *International Energy Outlook 2007, DOE/EIA-0484* **2007**, 19–27.
- (3) Liu, C.; Sakimoto, K. K.; Colon, B. C.; Silver, P. A.; Nocera, D. G. Ambient nitrogen reduction cycle using a hybrid inorganic-biological system. *Proc. Natl. Acad. Sci. U. S. A.* **2017**, *114* (25), 6450–6455.
- (4) Guo, C.; Ran, J.; Vasileff, A.; Qiao, S.-Z. Rational design of electrocatalysts and photo(electro)catalysts for nitrogen reduction to ammonia (NH<sub>3</sub>) under ambient conditions. *Energy Environ. Sci.* **2018**, *11* (1), 45–56.
- (5) White, J. L.; Baruch, M. F.; Pander, J. E., III; Hu, Y.; Fortmeyer, I. C.; Park, J. E.; Zhang, T.; Liao, K.; Gu, J.; Yan, Y.; Shaw, T. W.; Abelev, E.; Bocarsly, A. B. Light-Driven Heterogeneous Reduction of Carbon Dioxide: Photocatalysts and Photoelectrodes. *Chem. Rev.* **2015**, *115* (23), 12888–935.
- (6) Yan, Y.; Zeitler, E. L.; Gu, J.; Hu, Y.; Bocarsly, A. B. Electrochemistry of aqueous pyridinium: exploration of a key aspect of electrocatalytic reduction of CO<sub>2</sub> to methanol. *J. Am. Chem. Soc.* **2013**, *135* (38), 14020–3.
- (7) Nitopi, S.; Bertheussen, E.; Scott, S. B.; Liu, X.; Engstfeld, A. K.; Horch, S.; Seger, B.; Stephens, I. E. L.; Chan, K.; Hahn, C.; Norskov, J. K.; Jaramillo, T. F.; Chorkendorff, I. Progress and Perspectives of Electrochemical CO<sub>2</sub> Reduction on Copper in Aqueous Electrolyte. *Chem. Rev.* **2019**, *119*, 7610–7672.
- (8) Gu, J.; Yan, Y.; Young, J. L.; Steirer, K. X.; Neale, N. R.; Turner, J. A. Water reduction by a p-GaInP<sub>2</sub> photoelectrode stabilized by an amorphous TiO<sub>2</sub> coating and a molecular cobalt catalyst. *Nat. Mater.* **2016**, *15* (4), 456–60.
- (9) Gu, J.; Yan, Y.; Krizan, J. W.; Gibson, Q. D.; Detweiler, Z. M.; Cava, R. J.; Bocarsly, A. B. p-type CuRhO<sub>2</sub> as a self-healing photoelectrode for water reduction under visible light. *J. Am. Chem. Soc.* **2014**, *136* (3), 830–3.
- (10) Chen, X.; Aschaffenburg, D. J.; Cuk, T. Selecting between two transition states by which water oxidation intermediates decay on an oxide surface. *Nat. Catal.* **2019**, *2* (9), 820–827.
- (11) Oelgemoller, M. Solar Photochemical Synthesis: From the Beginnings of Organic Photochemistry to the Solar Manufacturing of Commodity Chemicals. *Chem. Rev.* **2016**, *116* (17), 9664–82.
- (12) Zhang, T.; Lin, W. Metal-organic frameworks for artificial photosynthesis and photocatalysis. *Chem. Soc. Rev.* **2014**, *43* (16), 5982–93.
- (13) Savateev, A.; Ghosh, I.; König, B.; Antonietti, M. Photoredox Catalytic Organic Transformations using Heterogeneous Carbon Nitrides. *Angew. Chem., Int. Ed.* **2018**, *57* (49), 15936–15947.
- (14) Ghosh, I.; Khamrai, J.; Savateev, A.; Shlapakov, N.; Antonietti, M.; König, B. Organic semiconductor photocatalyst can bifunctionalize arenes and heteroarenes. *Science* **2019**, *365* (6451), 360.
- (15) Jiang, Y.; Wang, C.; Rogers, C. R.; Kodaimati, M. S.; Weiss, E. A. Regio- and diastereoselective intermolecular [2 + 2] cycloadditions photocatalysed by quantum dots. *Nat. Chem.* **2019**, *11* (11), 1034–1040.
- (16) Caputo, J. A.; Frenette, L. C.; Zhao, N.; Sowers, K. L.; Krauss, T. D.; Weix, D. J. General and Efficient C-C Bond Forming Photoredox Catalysis with Semiconductor Quantum Dots. *J. Am. Chem. Soc.* **2017**, *139* (12), 4250–4253.
- (17) Cherevatskaya, M.; Neumann, M.; Fuldner, S.; Harlander, C.; Kummel, S.; Dankesreiter, S.; Pfitzner, A.; Zeitler, K.; König, B. Visible-light-promoted stereoselective alkylation by combining heterogeneous photocatalysis with organocatalysis. *Angew. Chem., Int. Ed.* **2012**, *51* (17), 4062–6.
- (18) Zhu, X.; Lin, Y.; Sun, Y.; Beard, M. C.; Yan, Y. Lead-Halide Perovskites for Photocatalytic alpha-Alkylation of Aldehydes. *J. Am. Chem. Soc.* **2019**, *141* (2), 733–738.
- (19) Lu, H.; Zhu, X.; Miller, C.; San Martin, J.; Chen, X.; Miller, E. M.; Yan, Y.; Beard, M. C. Enhanced photoredox activity of CsPbBr<sub>3</sub> nanocrystals by quantitative colloidal ligand exchange. *J. Chem. Phys.* **2019**, *151* (20), 204305.
- (20) Wang, K.; Lu, H.; Zhu, X.; Lin, Y.; Beard, M. C.; Yan, Y.; Chen, X. Ultrafast Reaction Mechanisms in Perovskite Based Photocatalytic C-C Coupling. *ACS Energy Lett.* **2020**, *5* (2), 566–571.
- (21) Zhu, X.; Lin, Y.; San Martin, J.; Sun, Y.; Zhu, D.; Yan, Y. Lead halide perovskites for photocatalytic organic synthesis. *Nat. Commun.* **2019**, *10* (1), 2843.
- (22) Wu, W.-B.; Wong, Y.-C.; Tan, Z.-K.; Wu, J. Photo-induced thiol coupling and C-H activation using nanocrystalline lead-halide perovskite catalysts. *Catal. Sci. Technol.* **2018**, *8* (16), 4257–4263.
- (23) Feng, H. J.; Paudel, T. R.; Tsybalyk, E. Y.; Zeng, X. C. Tunable Optical Properties and Charge Separation in CH<sub>3</sub>NH<sub>3</sub>Sn<sub>(x)</sub>Pb<sub>(1-x)</sub>I<sub>3</sub>/TiO<sub>2</sub>-Based Planar Perovskites Cells. *J. Am. Chem. Soc.* **2015**, *137* (25), 8227–36.
- (24) Nedelcu, G.; Protesescu, L.; Yakunin, S.; Bodnarchuk, M. I.; Grotevent, M. J.; Kovalenko, M. V. Fast Anion-Exchange in Highly Luminescent Nanocrystals of Cesium Lead Halide Perovskites (CsPbX<sub>3</sub>, X = Cl, Br, I). *Nano Lett.* **2015**, *15* (8), 5635–40.
- (25) Chiba, T.; Hayashi, Y.; Ebe, H.; Hoshi, K.; Sato, J.; Sato, S.; Pu, Y.-J.; Ohisa, S.; Kido, J. Anion-exchange red perovskite quantum dots with ammonium iodine salts for highly efficient light-emitting devices. *Nat. Photonics* **2018**, *12* (11), 681–687.
- (26) Hazarika, A.; Zhao, Q.; Gauding, E. A.; Christians, J. A.; Dou, B.; Marshall, A. R.; Moot, T.; Berry, J. J.; Johnson, J. C.; Luther, J. M. Perovskite Quantum Dot Photovoltaic Materials beyond the Reach of



Thin Films: Full-Range Tuning of A-Site Cation Composition. *ACS Nano* **2018**, *12* (10), 10327–10337.

(27) Semonin, O. E.; Luther, J. M.; Choi, S.; Chen, H.-Y.; Gao, J.; Nozik, A. J.; Beard, M. C. Peak External Photocurrent Quantum Efficiency Exceeding 100% via MEG in a Quantum Dot Solar Cell. *Science* **2011**, *334* (6062), 1530.

(28) Bi, C.; Wang, S.; Li, Q.; Kershaw, S. V.; Tian, J.; Rogach, A. L. Thermally Stable Copper(II)-Doped Cesium Lead Halide Perovskite Quantum Dots with Strong Blue Emission. *J. Phys. Chem. Lett.* **2019**, *10* (5), 943–952.

(29) Zhang, Y.; Lu, D.; Gao, M.; Lai, M.; Lin, J.; Lei, T.; Lin, Z.; Quan, L. N.; Yang, P. Quantitative imaging of anion exchange kinetics in halide perovskites. *Proc. Natl. Acad. Sci. U. S. A.* **2019**, *116* (26), 12648–12653.

(30) Creutz, S. E.; Crites, E. N.; De Siena, M. C.; Gamelin, D. R. Anion Exchange in Cesium Lead Halide Perovskite Nanocrystals and Thin Films Using Trimethylsilyl Halide Reagents. *Chem. Mater.* **2018**, *30* (15), 4887–4891.

(31) Sygletou, M.; Kyriazi, M. E.; Kanaras, A. G.; Stratakis, E. Anion exchange in inorganic perovskite nanocrystal polymer composites. *Chem. Sci.* **2018**, *9* (42), 8121–8126.

(32) Skubi, K. L.; Blum, T. R.; Yoon, T. P. Dual Catalysis Strategies in Photochemical Synthesis. *Chem. Rev.* **2016**, *116* (17), 10035–10074.

(33) van der Stam, W.; Geuchies, J. J.; Altantzis, T.; van den Bos, K. H. W.; Meeldijk, J. D.; Van Aert, S.; Bals, S.; Vanmaekelbergh, D.; de Mello Donega, C. Highly Emissive Divalent-Ion-Doped Colloidal CsPb<sub>1-x</sub>MxBr<sub>3</sub> Perovskite Nanocrystals through Cation Exchange. *J. Am. Chem. Soc.* **2017**, *139* (11), 4087–4097.

(34) Chen, Y.-C.; Chou, H.-L.; Lin, J.-C.; Lee, Y.-C.; Pao, C.-W.; Chen, J.-L.; Chang, C.-C.; Chi, R.-Y.; Kuo, T.-R.; Lu, C.-W.; Wang, D.-Y. Enhanced Luminescence and Stability of Cesium Lead Halide Perovskite CsPbX<sub>3</sub> Nanocrystals by Cu<sup>2+</sup>-Assisted Anion Exchange Reactions. *J. Phys. Chem. C* **2019**, *123* (4), 2353–2360.

(35) Prier, C. K.; Rankic, D. A.; MacMillan, D. W. Visible light photoredox catalysis with transition metal complexes: applications in organic synthesis. *Chem. Rev.* **2013**, *113* (7), 5322–63.

(36) Romero, N. A.; Nicewicz, D. A. Organic Photoredox Catalysis. *Chem. Rev.* **2016**, *116* (17), 10075–166.

(37) Sonobe, T.; Oisaki, K.; Kanai, M. Catalytic aerobic production of imines en route to mild, green, and concise derivatizations of amines. *Chem. Sci.* **2012**, *3* (11), 3249–3255.

(38) Cui, X.; Li, Y.; Bachmann, S.; Scalone, M.; Surkus, A. E.; Junge, K.; Topf, C.; Beller, M. Synthesis and Characterization of Iron-Nitrogen-Doped Graphene/Core-Shell Catalysts: Efficient Oxidative Dehydrogenation of N-Heterocycles. *J. Am. Chem. Soc.* **2015**, *137* (33), 10652–10658.

(39) Zhang, Y.; Duan, D.; Zhong, Y.; Guo, X. A.; Guo, J.; Gou, J.; Gao, Z.; Yu, B. Fe(III)-Catalyzed Aerobic Intramolecular N-N Coupling of Aliphatic Azides with Amines. *Org. Lett.* **2019**, *21* (13), 4960–4965.

(40) Zhang, C.; Jiao, N. Copper-catalyzed aerobic oxidative dehydrogenative coupling of anilines leading to aromatic azo compounds using dioxygen as an oxidant. *Angew. Chem., Int. Ed.* **2010**, *49* (35), 6174–7.

(41) Zhu, Y.; Shi, Y. Facile Cu(I)-Catalyzed Oxidative Coupling of Anilines to Azo Compounds and Hydrazines with Diaziridinone under Mild Conditions. *Org. Lett.* **2013**, *15* (8), 1942–1945.

(42) Rosen, B. R.; Werner, E. W.; O'Brien, A. G.; Baran, P. S. Total synthesis of dixiamycin B by electrochemical oxidation. *J. Am. Chem. Soc.* **2014**, *136* (15), 5571–5574.

(43) Ryan, M. C.; Martinelli, J. R.; Stahl, S. S. Cu-Catalyzed Aerobic Oxidative N-N Coupling of Carbazoles and Diarylamines Including Selective Cross-Coupling. *J. Am. Chem. Soc.* **2018**, *140* (29), 9074–9077.

(44) Bouduban, M. E. F.; Burgos-Caminal, A.; Ossola, R.; Teuscher, J.; Moser, J.-E. Energy and charge transfer cascade in methylammonium lead bromide perovskite nanoparticle aggregates. *Chem. Sci.* **2017**, *8* (6), 4371–4380.

(45) Li, J.; Zhang, Z.; Wu, L.; Zhang, W.; Chen, P.; Lin, Z.; Liu, G. Site-specific allylic C-H bond functionalization with a copper-bound N-centred radical. *Nature* **2019**, *574* (7779), 516–521.

(46) Wu, K.; Liang, G.; Shang, Q.; Ren, Y.; Kong, D.; Lian, T. Ultrafast Interfacial Electron and Hole Transfer from CsPbBr<sub>3</sub> Perovskite Quantum Dots. *J. Am. Chem. Soc.* **2015**, *137* (40), 12792–12795.

(47) Gao, Y.; Zhang, P.; Ji, Z.; Tang, G.; Zhao, Y. Copper-Catalyzed Cascade Radical Addition-Cyclization Halogen Atom Transfer between Alkynes and Unsaturated  $\alpha$ -Halogenocarbonyls. *ACS Catal.* **2017**, *7* (1), 186–190.

(48) Gieshoff, T.; Schollmeyer, D.; Waldvogel, S. R. Access to Pyrazolidin-3,5-diones through Anodic N-N Bond Formation. *Angew. Chem., Int. Ed.* **2016**, *55* (32), 9437–40.

(49) Gieshoff, T.; Kehl, A.; Schollmeyer, D.; Moeller, K. D.; Waldvogel, S. R. Insights into the Mechanism of Anodic N-N Bond Formation by Dehydrogenative Coupling. *J. Am. Chem. Soc.* **2017**, *139* (35), 12317–12324.

(50) Grirrane, A.; Corma, A.; García, H. Gold-Catalyzed Synthesis of Aromatic Azo Compounds from Anilines and Nitroaromatics. *Science* **2008**, *322* (5908), 1661.

(51) Ke, L.; Zhu, G.; Qian, H.; Xiang, G.; Chen, Q.; Chen, Z. Catalytic Selective Oxidative Coupling of Secondary N-Alkylanilines: An Approach to Azoxyarene. *Org. Lett.* **2019**, *21* (11), 4008–4013.

(52) Dean, C.; Rajkumar, S.; Roesner, S.; Carson, N.; Clarkson, G. J.; Wills, M.; Jones, M.; Shipman, M. Readily accessible sp<sup>3</sup>-rich cyclic hydrazine frameworks exploiting nitrogen fluxionality. *Chem. Sci.* **2020**, *11* (6), 1636–1642.

(53) Nykaza, T. V.; Harrison, T. S.; Ghosh, A.; Putnik, R. A.; Radosevich, A. T. A Biphilic Phosphetane Catalyzes N-N Bond-Forming Cadogan Heterocyclization via P<sup>III</sup>/P<sup>V</sup>=O Redox Cycling. *J. Am. Chem. Soc.* **2017**, *139* (20), 6839–6842.

(54) Ueda, S.; Nagasawa, H. Facile Synthesis of 1,2,4-Triazoles via a Copper-Catalyzed Tandem Addition-Oxidative Cyclization. *J. Am. Chem. Soc.* **2009**, *131* (42), 15080–15081.

(55) Dai, G.; Yang, L.; Zhou, W. Copper-catalyzed oxidative dehydrogenative N-N bond formation for the synthesis of N,N'-diarylindazol-3-ones. *Org. Chem. Front.* **2017**, *4* (2), 229–231.

(56) Neumann, J. J.; Suri, M.; Glorius, F. Efficient Synthesis of Pyrazoles: Oxidative C-C/N-N Bond-Formation Cascade. *Angew. Chem., Int. Ed.* **2010**, *49* (42), 7790–7794.

(57) Hirayama, T.; Ueda, S.; Okada, T.; Tsurue, N.; Okuda, K.; Nagasawa, H. Facile One-Pot Synthesis of [1, 2, 3]Triazolo[1, 5-a]pyridines from 2-Acylpyridines by Copper(II)-Catalyzed Oxidative N-N Bond Formation. *Chem. - Eur. J.* **2014**, *20* (14), 4156–4162.

(58) Hu, J.; Cheng, Y.; Yang, Y.; Rao, Y. A general and efficient approach to 2H-indazoles and 1H-pyrazoles through copper-catalyzed intramolecular N-N bond formation under mild conditions. *Chem. Commun.* **2011**, *47* (36), 10133–10135.

(59) Huang, H.; Cai, J.; Ji, X.; Xiao, F.; Chen, Y.; Deng, G.-J. Internal Oxidant-Triggered Aerobic Oxygenation and Cyclization of Indoles under Copper Catalysis. *Angew. Chem., Int. Ed.* **2016**, *55* (1), 307–311.

(60) Yu, D.-G.; Suri, M.; Glorius, F. RhIII/CuII-Cocatalyzed Synthesis of 1H-Indazoles through C-H Amidation and N-N Bond Formation. *J. Am. Chem. Soc.* **2013**, *135* (24), 8802–8805.

(61) Chen, C.-Y.; Tang, G.; He, F.; Wang, Z.; Jing, H.; Faessler, R. A Synthesis of 1H-Indazoles via a Cu(OAc)<sub>2</sub>-Catalyzed N-N Bond Formation. *Org. Lett.* **2016**, *18* (7), 1690–1693.